Publication II

J. Heiskala, P. Hiltunen and I. Nissilä. Significance of background optical properties and time-resolved information in diffuse optical imaging of term neonates. *Physics in Medicine and Biology*, 54(3), 535–554, 2009.

IOP PUBLISHING PHYSICS IN MEDICINE AND BIOLOGY

Phys. Med. Biol. **54** (2009) 535–554 doi:10.1088/0031-9155/54/3/005

Significance of background optical properties, time-resolved information and optode arrangement in diffuse optical imaging of term neonates

J Heiskala[1,2], **P Hiltunen**[2] **and I Nissilä**[2,3]

[1] BioMag Laboratory, HUSLAB, Helsinki University Central Hospital, PO Box 340, FI-00029 HUS, Finland
[2] Department of Biomedical Engineering and Computational Science, Helsinki University of Technology, PO Box 3310, FI-02015 HUT, Finland
[3] Institute for Biomedicine, University of Helsinki, Biomedicum Helsinki, FI-00014 HY, Finland

E-mail: Juha.Heiskala@iki.fi

Received 3 July 2008, in final form 16 November 2008
Published 6 January 2009
Online at stacks.iop.org/PMB/54/535

Abstract

The significance of accurate knowledge of background optical properties and time-resolved information in reconstructing images of hemodynamic changes in the neonatal brain from diffuse optical imaging data was studied using Monte Carlo (MC) simulation. A segmented anatomical magnetic resonance (MR) image and literature-derived optical properties for each tissue type were used to create a voxel-based anatomical model. Small absorbing perturbations were introduced into the anatomical model to simulate localized hemodynamic responses related to brain activation. Perturbation MC (pMC) was used as the primary method of image reconstruction. For comparison, reconstructions were also performed using the finite element method (FEM) to solve the diffusion approximation (DA) to the radiative transfer equation (RTE). The effect of optode layout was investigated using three different grids. Of the factors studied, the density of the optode grid was found to have the greatest effect on image quality. The use of time-resolved information significantly improved the spatial accuracy with all optode grids. Adequate knowledge and modeling of the optical properties of the background was found to significantly improve the spatial accuracy of the reconstructed images and make the recovery of contrast of absorption changes more consistent over simplified modeling. Localization accuracy of small perturbations was found to be 2–3 mm with accurate *a priori* knowledge of the background optical properties, when a grid with high optode density (>1 optode cm^{-2}) was used.

1. Introduction

In the last two decades, rapid development of methods for non-invasive functional imaging of the human brain has taken place. Macroscopic currents closely related to neuronal activity can be estimated from non-invasive measurements made with electroencephalography (EEG) and magnetoencephalography (MEG, Hämäläinen *et al* 1993). Due to the increased metabolic demand in activated areas, local blood flow is normally increased through the neurovascular coupling to provide adequate supply. Increased blood flow results in increased local concentration of oxygenated hemoglobin (HbO_2) and, in the adult, decreased concentration of deoxyhemoglobin (HbR). Hemodynamic responses can be imaged using functional magnetic resonance imaging (fMRI; Rosen *et al* 1993), positron emission tomography (PET), single-photon emission computed tomography (SPECT) and near-infrared spectroscopy (NIRS; Villringer and Chance 1997). The hemodynamic signals are a more indirect measure of neuronal activity than the primary current distribution estimated from MEG and EEG, but the spatial resolution can be very good. In addition to neuroscientific studies, measurements of hemodynamic parameters can also be used to detect and image lesions in the brain.

In order to diagnose developmental problems in infants, one possibility is to study the infant development using a variety of neuroimaging methods to create a reference database, and then compare individual patient results with this normative data. Neuroimaging of infants is very challenging. Changes in the sleep stage and attentive state are frequent. MRI and fMRI in general require sedation, which can alter neuronal and hemodynamic responses and limits the types of tasks that can be used. Near-infrared spectroscopy (NIRS) and imaging (NIRSI) (Villringer and Chance 1997) are safe methods which allow the determination of changes in the concentration of HbO_2 and HbR in the infant brain (Hebden *et al* 2004, Gibson *et al* 2006). The thin structures of the skull and scalp of a neonate enhance the applicability of optical methods. In preterm infants, it may even be possible to perform optical measurements through the entire head to obtain three-dimensional tomographic images. The instrumentation needed for NIRSI is relatively light and quiet, and the measurement can be performed at the bedside.

Image reconstruction from optical measurements is sensitive to the modeling of light transport in tissue. The radiative transfer equation (RTE; Chandrasekhar, 1960) is a general model which is thought to accurately model light propagation in tissue. The diffusion approximation (DA) to the RTE can be used to model light propagation in the brain, skull and skin tissues (Arridge 1999). The cerebrospinal fluid (CSF) is a clear liquid which shares its space with blood vessels and the delicate network of thin fibers of the arachnoid mater. Because of these structures, the CSF space is not completely non-scattering, but it is reasonable to assume that the scattering coefficient in the CSF space is low. Large low-scattering regions result in photon propagation which cannot be accurately modeled by the DA. Several approaches have been proposed for modeling the CSF, including Monte Carlo (MC) simulation (Firbank *et al* 1996, Okada *et al* 1997), a hybrid radiosity diffusion FEM model which assumes the CSF to be non-scattering (Okada *et al* 1997, Dehghani *et al* 2000, Riley *et al* 2000, Dehghani and Delpy 2002, Gibson *et al* 2005), numerical solutions to the RTE itself (Ren *et al* 2004), as well as a hybrid RTE–DA method (Tarvainen *et al* 2005). In this study, we used a low-scattering coefficient (μ_s), which we think is a plausible model for large regions of CSF, although no direct *in situ* measurements of $\mu_{s,CSF}$ have been presented in the literature.

The optical imaging of brain activation in term infants is different from studies with preterm infant and adult subjects. In term infants and adults, the strong attenuation of the optical signal limits measurements to relatively short source–detector distances ($\leqslant 50$ mm), whereas in preterm infants optical measurements through the entire head may be possible.

Compared to adult subjects, the neonatal cortex is much closer to the surface of the head, which makes higher resolution and more consistent contrast recovery possible. The effect of the heterogeneous structure of the head on image quality in activation studies of term infants has not previously been studied. The fact that the distance from the optodes to the brain is typically only a few millimeters needs to be considered in the grid design.

In the present study, we investigated the significance of errors in the model of light propagation and background optical properties in reconstructing three-dimensional images from the optical imaging of brain activations in term neonates. We were specifically interested in changes in the concentration of oxygenated haemoglobin, which are exhibited as changes in optical absorption in the brain. We also studied the effect of the choice of the optode grid and the availability of time-resolved information on the quality of reconstructed images. Our results should be helpful for planning future experiments and the selection of modeling and image reconstruction approaches.

MC simulation (Prahl *et al* 1989) was used to generate the simulated data in this study because of the straightforward adaptability to arbitrary tissue geometries and optical properties. The tissue geometry was taken from an anatomical MR image of a term neonate, which was segmented into tissue classes. Literature-based optical properties were assigned to the tissue classes. For image reconstruction using MC, we implemented a perturbation Monte Carlo (pMC) (Hayakawa *et al* 2001, Kumar and Vasu 2004) method using mean time and intensity data types. MC-based methods have not previously been used to image neonates, nor has mean time been used for image reconstruction with an MRI-based realistic heterogeneous model of the head.

Our results show that deviations from the correct background properties change the reconstructed image significantly. This change may be a loss of contrast or an error in the reconstructed position of the perturbation. It is thus important to take advantage of all available *a priori* information on the background optical properties. A comparison of reconstructions based on (1) MC with precisely correct background properties, (2) MC with the optical properties of the CSF replaced by the properties of weakly diffuse tissue ($\mu_s' = 0.3\ \mathrm{mm}^{-1}$), (3) MC with deviated background properties, (4) MC with homogeneous background properties, (5) the FEM/DA with the properties of the CSF replaced by the properties of diffuse tissue and (6) the FEM/DA with homogeneous optical properties is shown.

The use of time-of-flight information in image reconstruction in optical tomography has been studied both theoretically and experimentally (Arridge 1999). The most important benefit from the use of temporal data types is the ability to differentiate between scattering and absorption in the tissue (Arridge and Lionheart 1998). Time-resolved data types such as the mean time and variance, and time-gated windows of the temporal point spread function have been used to separate functional changes that occur in layers at different depths in the tissue (Steinbrink *et al* 2001, Liebert *et al* 2004, Selb *et al* 2006). Experimental data from time domain (TD) and frequency domain (FD) optical imaging in adults (Toronov *et al* 2001) as well as in infants (Chance *et al* 1998, Heiskala *et al* 2007) suggest that the mean time (TD) and phase (FD) can be used to detect brain activation. Our results show that time-resolved information can also help to improve the spatial accuracy of reconstructions parallel to the surface of the scalp.

Three different spatial arrangements of optical fibers were compared, the so-called hexagonal arrangement (Boas and Dale 2005), the 'double-density' (DD) grid (Kawaguchi *et al* 2007) and a high-density (HD) grid similar to that used by Zeff *et al* (2007). All grids were scaled down to account for the smaller head size of the infant. The quality of the image, including contrast and resolution, was evaluated with and without the mean time data. The optode density was found to be the most significant factor affecting reconstructed image quality.

2. Methods

2.1. The Monte Carlo method

We employed the MC method to simulate photon propagation in the tissue and to obtain sensitivity maps that provide an estimate of the change in the optical signal in response to a change in the optical parameters at a specific location. In our implementation, the tissue model is described with the help of voxels (Boas *et al* 2002) that can have arbitrary dimensions.

2.1.1. Photon propagation. The rules of photon propagation are described in the literature (Prahl *et al* 1989, Wang *et al* 1995). The pathlength between two scattering events is drawn from the exponential probability density $\mu_s \exp(-\mu_s L)$, and absorption is handled by multiplication of the weight of a photon packet by $\exp(-\mu_a L)$, where μ_s and μ_a are the scattering and absorption coefficients, and L is the pathlength of a photon packet between scattering events. Situations in which a photon packet passes from one tissue type to another with different optical properties require special treatment, and are handled as described by Boas *et al* (2002).

We used point sources and circular detectors with a radius of 2 mm, which allowed us to record approximately 2 photon packets out of 1000 launched at a detector located 12.5 mm from the source. The actual numbers naturally depended on the location in the optode grid and the optical properties used.

2.1.2. Perturbation Monte Carlo. In the pMC method, paths of photon packets from MC simulation are used to calculate the derivative of the forward model with respect to optical parameters (Frechet derivatives). This allows creating three-dimensional sensitivity maps which can be used to estimate the change in the optical signal in response to a change in the optical parameters at a given location. In the present study, we only consider perturbations in absorption. The motivation for this choice was that in the literature of NIRS studies of brain activations, it is commonly assumed that changes occur mainly in absorption, and that the concentrations of oxyhemoglobin and deoxyhemoglobin can be estimated from changes in the absorption coefficient for different wavelengths (Steinbrink *et al* 2001, Boas *et al* 2004, Kacprzak *et al* 2007). Considering changes in scattering using the pMC method is also possible (Hayakawa *et al* 2001, Kumar and Vasu 2004), but this is beyond the scope of this paper.

The signal intensity W and the mean time of flight of photons $\langle t \rangle$ are obtained from the MC simulation as follows.

The signal intensity seen by a detector is given by

$$W = \sum_p w_p = \sum_p \exp\left(-\sum_r \mu_a(r) l_{r,p}\right), \tag{1}$$

where w_p is the intensity contribution of the photon packet p, and $\mu_a(r)$ and $l_{r,p}$ are the absorption coefficient and the path length of the photon packet p in the region r of the tissue, respectively. The sum in the exponential function goes over all regions r.

The average photon flight time is given by (Steinbrink *et al* 2001)

$$\langle t \rangle = \frac{\sum_p t_p w_p}{\sum_p w_p} = \frac{\sum_p t_p \exp\left(-\sum_r \mu_a(r) l_{r,p}\right)}{\sum_p \exp\left(-\sum_r \mu_a(r) l_{r,p}\right)}, \tag{2}$$

where the total flight time t_p of the photon packet is the sum $t_p = \sum_\rho t_{p,\rho}$ of the flight times $t_{p,\rho}$ in all regions ρ.

The sensitivity of the signal to a change in μ_a in a region ρ is obtained by differentiation. For the intensity, we obtain (Hiraoka *et al* 1993)

$$\frac{\partial W}{\partial \mu_a(\rho)} = \sum_p -l_{\rho,p} \exp\left(-\sum_r \mu_a(r) l_{r,p}\right) = \langle l_\rho \rangle W, \tag{3}$$

where $\langle l_\rho \rangle$ is the average weighted photon pathlength in the region ρ.

Differentiation of formula (2) yields (Arridge 1995, Steinbrink *et al* 2001)

$$\frac{\partial \langle t \rangle}{\partial \mu_a(\rho)} = -\langle l_\rho t \rangle + \langle l_\rho \rangle \langle t \rangle, \tag{4}$$

where $\langle l_\rho t \rangle$ is the average pathlength of the photon packets in the region ρ, weighted with the total flight time and the final weight of the photon packets at the detector.

Formulae (3) and (4) are first derivatives and represent the linear response to changes in absorption in individual regions. Higher-order approximations involving expectation values of cross terms $\langle l_i l_j \rangle$ between photon pathlengths in different regions have been presented in the literature (see, for example, Steinbrink *et al* 2001 or Tsuchiya 2001). We use only the linear terms, because in our high-resolution application, the number of regions r is of the order of 50 000, and storing N^2 cross terms for each measurement is not feasible.

We use stored sensitivity maps obtained from MC simulation for reconstructing changes in absorption from changes in the optical signal. This avoids repeatedly calculating the computationally costly MC forward solution. In using stored maps of sensitivity, we make the approximation that the sensitivity profile is not significantly altered by the changes induced in the optical properties. Our results indicate that this linear approximation is sufficiently accurate for image reconstruction in the case of localized μ_a changes such as those studied in this paper. Work by Liebert *et al* (2004) suggests that linear methods may also be appropriate for estimating absorption changes over larger volumes in the brain.

The reconstruction is done by minimizing the objective function,

$$\Phi(\Delta\vec{\mu}_a) = \alpha A(\Delta\vec{\mu}_a) + \beta B(\Delta\vec{\mu}_a) + \gamma_1 R_1(\Delta\vec{\mu}_a) + \gamma_2 R_2(\Delta\vec{\mu}_a), \tag{5}$$

where the vector $\Delta\vec{\mu}_a$ represents the change in μ_a in different voxels of the imaged volume.

$A(\Delta\vec{\mu}_a)$ and $B(\Delta\vec{\mu}_a)$ are given by

$$A(\Delta\vec{\mu}_a) = \sum_{s,d}\left(\frac{1}{\sigma^2_{\log[I_{EXP}]}(s,d)}\left(\Delta\log[I_{pMC}(s,d,\Delta\vec{\mu}_a)] - \Delta\log[I_{EXP}(s,d)]\right)^2\right) \tag{6}$$

$$B(\Delta\vec{\mu}_a) = \sum_{s,d}\left(\frac{1}{\sigma^2_{\langle t\rangle_{EXP}}(s,d)}(\Delta\langle t\rangle_{pMC}(s,d,\Delta\vec{\mu}_a) - \Delta\langle t\rangle_{EXP}(s,d))^2\right), \tag{7}$$

where the sum goes over all source–detector pairs (s,d). $A(\Delta\vec{\mu}_a)$ and $B(\Delta\vec{\mu}_a)$ are calculated as sums of the square of the difference between the model-predicted (subscript pMC) and measured (subscript EXP) changes in the intensity and the mean time-of-flight data types, weighted by the reciprocal of the variance of the measurements. For our simulated case, we divided the data into bins and calculated the variance between these.

When using both mean time and intensity data, we set α and β so that both $\alpha A(\Delta\vec{\mu}_a) = \beta B(\Delta\vec{\mu}_a) = 1.0$. In the intensity-only case, we initialized $\alpha A(\Delta\vec{\mu}_a)$ to 2.0.

The functions $R_1(\Delta\vec{\mu}_a)$ and $R_2(\Delta\vec{\mu}_a)$ are regularization functions. $R_1(\Delta\vec{\mu}_a)$ is simply the norm of the solution vector:

$$R_1(\Delta\vec{\mu}_a) = \|\Delta\vec{\mu}_a\|_2^2, \tag{8}$$

or Tikhonov regularization. The second regularization function is given by

$$R_2 = \|\mathbf{L}\Delta\vec{\mu}_a\|_2^2, \tag{9}$$

where $\mathbf{L}$ is defined by

$$L_{ij} = \begin{cases} nn, & \text{if} \quad i = j \\ -1, & \text{if} \quad j \text{ is a neighbor of } i, \\ 0 & \text{otherwise} \end{cases}$$

where nn is the number of neighbors of voxel i (26-neighborhood was used).

The second regularization term is used to reduce the high-frequency noise present in the unregularized reconstructions.

The regularization parameters were chosen empirically for each optode grid. The quality index (see section 2.5) calculated from the reconstructed images and visual appraisal of the images were used in determining optimal regularization parameters. The γ_1 parameter was chosen large enough to suppress artifacts caused by the photon noise, but not larger, as this would reduce the contrast of the reconstructions. γ_2 was set to limit the high-frequency noise in the reconstructed image. For a given optode grid, the regularization was held constant for all the different perturbation positions and background models. The regularization parameters for the optode grids introduced in section 2.4 were ($\gamma_1 = 2.5\ \text{mm}^2, \gamma_2 = 1.0\ \text{mm}^2$) for the hexagonal grid, ($\gamma_1 = 2.3\ \text{mm}^2, \gamma_2 = 0.8\ \text{mm}^2$) for the double-density grid and ($\gamma_1 = 1.5\ \text{mm}^2, \gamma_2 = 1.5\ \text{mm}^2$) for the high-density grid.

The reconstruction is performed by an iterative algorithm which consists in calculating the gradient of Φ with respect to $\vec{\mu}_a$ and performing a line search to find the $\vec{\mu}_a$ that minimizes the objective function. After updating the functions A, B, R_1 and R_2, a new gradient is calculated and a new line search is performed. The iteration is repeated until one of the following conditions is met: (I) a (local) minimum of the objective function is found, (II) the objective function becomes smaller than a pre-defined threshold, or (III) a pre-defined maximum number of cycles has been performed.

2.2. The finite element method

The numerical solution of the DA using the FEM is a widely used method of modeling in optical tomography. We therefore compared the results from our pMC-based reconstruction algorithm to those obtained using a FEM-based forward model. For details on using the FEM to solve the DA, see Arridge (1999) and Schweiger *et al* (2005).

The FEM-based image reconstruction was done by minimizing an objective function which was identical to that given in equation (5), described above, except for the regularization. The first regularization term was as in the MC case, and the regularization parameter was chosen using the same criteria as in the pMC case. It was set to $\gamma = 0.15\ \text{mm}^2$ for the hexagonal and double-density grids, and to $\gamma = 0.08\ \text{mm}^2$ for the high-density grid. The second regularization term R_2 was not used since the FEM reconstructions did not exhibit high-frequency noise.

Damped Gauss–Newton iteration with quadratic fit line search was used to minimize the objective function (Bazaraa *et al* 1993, Björck 1996).

We studied (1) the case of the FEM/DA with heterogeneous optical parameters that were set to correspond to the voxel-based model as closely as the mesh resolution allowed and (2)

Table 1. Optical properties of tissue types (Schmidt 1999, Fukui *et al* 2003).

Tissue type	μ_s' (mm^{-1})	g	μ_a (mm^{-1})	n
Scalp	1.9	0.9	0.018	1.3
Skull	1.6	0.9	0.016	1.3
Gray matter	0.5	0.9	0.048	1.3
White matter	1.0	0.9	0.037	1.3
CSF	0.032	0.9	0.0041	1.3

the FEM/DA with homogeneous parameters. The heterogeneous parameters were obtained by sampling the voxel-based head model. Since the assumptions made in deriving the DA are not valid in low-scattering regions, we used the weakly diffusive scattering parameter ($\mu_s' = 0.3$ mm^{-1}) suggested by Custo *et al* (2006) for the CSF in the FEM calculations.

2.3. The anatomical model

The anatomical model was derived from a T_1 MR image of a term neonate. The MR image was segmented into distinct tissue classes, the optical properties of which were taken from the literature. We assumed the CSF to be clear, with small but finite μ_s'. While the actual scattering properties of CSF regions are not well established, this allowed us to investigate the possible effect of a clear layer for activation imaging. The tissue classes and their optical properties are shown in table 1. The voxels in the MR image and consequently in the anatomical model were cubical with a side length of 0.86 mm.

For the FEM calculations, a mesh which matches the shape of the outer boundary of the voxel model was created. The mesh was optimized for FEM calculations in the region of the optode grid and contains 25 938 tetrahedral elements with quadratic basis functions and 40 012 nodes.

2.4. Optical fiber arrays

Three different arrangements of optical fibers were studied. These were the hexagonal grid proposed by Boas *et al* (2004), the double-density grid as proposed by Kawaguchi *et al* (2007) and a high-density grid similar to that used by Zeff *et al* (2007). All optode grids were scaled down in size to match the small size of the infant head. The hexagonal grid has the advantage of providing good topographic coverage of a larger area with a smaller number of source fibers, while the double-density grid offers, especially in the center of the grid, a large number of measurements with spatial overlap in the cortex. The DD grid features a dense mapping of the cortex with the 25 mm source–detector separation, which is often considered to provide an optimal contrast-to-noise ratio in activation imaging. The high-density grid has the most spatial overlap, but this has the drawback of requiring a large number of optodes.

The grids are illustrated in figure 1. The numbers of source and detector optodes are: hexagonal grid: 8 sources, 15 detectors; DD grid: 10 sources, 10 detectors and HD grid: 24 sources, 28 detectors. The DD grid is regular with an approximately 13 mm distance between neighboring optodes. In the hexagonal grid, the distance between the horizontal rows is approximately 12 mm, and the optodes on each row are placed at approximately 15 mm intervals. The HD grid has alternating horizontal rows of sources and detectors. The distance between the rows is approximately 8 mm, and the distance between the optodes in each row is 8.5 mm.

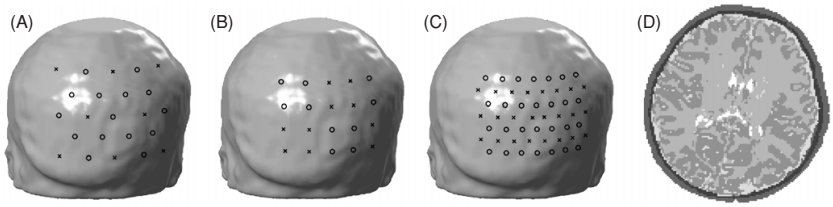

Figure 1. The layout of optodes in the hexagonal (A), DD (B) and HD (C) optode grids as used in the paper, and an axial view of the segmented head model (D). Sources are marked with 'X', and detectors are marked with 'O'.

2.5. Simulations

We used simulated data to study factors that potentially affect the image quality in the reconstruction of localized perturbations in the absorption coefficient. MC simulations were run with an absorbing perturbation or perturbations in place and without perturbations, and the differences in the simulated data were calculated. These difference data were then used in place of measurement data.

The voxel size in the sensitivity maps used for pMC reconstructions was ∼1.7 mm. The sensitivity maps had non-zero values in approximately 40 000–50 000 voxels depending on the optode grid and optical parameters.

The number of photon packets simulated was 800 million for each source for the hexagonal and DD grids, and 400 million for the HD grid. This choice was motivated by the necessarily shorter measurement time per source when using the HD grid. The standard errors in the intensity and time-of-flight measurements, and the corresponding phase shift at a modulation frequency of 100 MHz were approximately 0.2%, 0.2 ps and 0.007° at 12.5 mm source–detector separation, 0.7%, 1.4 ps and 0.05° at 25 mm and 2%, 10 ps and 0.4° at 40 mm. At the shortest source–detector separation of the HD grid the standard error in intensity was 0.1%.

The noise in the simulated data can be compared with the noise from our frequency-domain instrument (Nissilä *et al* 2005) in a practical activation imaging scenario. We used a phantom with optical characteristics of preterm infants and an adult volunteer subject to obtain the noise figures for using a multidistance grid with ten sources and ten detectors, with a 12 mm shortest distance between fibers. We assumed that 36 averages of the stimulus were available, and estimated the standard error of the mean from the data. At a relatively low source power of 1.5 mW and 40 ms switching time between source positions, the standard error was estimated to be 0.3–0.4% in amplitude and 0.1–0.2° in phase at a source–detector distance of 12 mm. At a 25 mm separation, the measured noise increased to 0.4–0.7% in amplitude and remained at 0.1°–0.2° in phase. At a 40 mm separation, the amplitude noise was 0.5–1.3% and the phase noise 1.5–5°. We conclude that the amplitude noise in a real measurement is comparable with the simulated noise, but the measured phase noise was higher especially at long source–detector distances. This difference can be attributed to instrument imperfections such as thermal drift, hysteresis (at short distances) and detector dark current (at long distances) which reduce the performance compared to an idealized system. At long distances, time-domain instruments such as the UCL system (Schmidt *et al* 2000) have lower noise in the mean time or phase (see Nissilä *et al* (2006) for a comparison). We think that our simulations have a noise level similar to what may be obtained in a practical measurement with a near-perfect instrument.

The average computation time for one source was approximately 25 h on an AMD Opteron (64 bit 2.0 GHz) processor using the optical parameters given in table 1. The computation time depended on the position of the simulated light source, varying from half the average time to almost double. A cluster of up to 25 nodes was used. In order to calculate the reconstructed images based on measured data, a smaller number of photon packets would be sufficient. Two hundred million photon packets (6 h computation time) was found to be acceptable to calculate the sensitivity maps for the image reconstruction. However, reducing the number of simulated photon packets to 80 million packets resulted in a clear increase of high-frequency noise in the reconstructed images. The computational time for the linear reconstruction is of the order of 15 min, depending on the optode grid. The method, while computationally heavy, is fast enough for the analysis of neuroscientific data.

Reconstructions were performed using (1) both intensity and mean time-of-flight information from TD data, as well as using (2) intensity data only.

To assess the quality of the reconstructed images, we calculated three different parameters from the images. These were the error in localization of the center of mass of the reconstructed perturbation, the peak contrast of the reconstructed perturbations and the image quality index (QI) explained below. We calculated the $\Delta\mu_{\mathrm{a}}$-weighted centers of mass for the three-dimensional 18 connected sets of voxels around the peaks of the reconstructed perturbations with $\Delta\mu_{\mathrm{a}}$ greater than 0.65 times the peak value, and compared these with the positions of the target perturbations. The cut-off value 0.65 was chosen because it allowed adjacent reconstructed perturbations to be treated as separate continuous regions in most cases. The QI was calculated by dividing the mean contrast in the target area by the standard deviation of the background. The background was defined as the volume below the optode grid down to the depth of the deepest part of the perturbations, excluding the target regions enlarged by increasing their original radius by a factor of 1.5 to allow for the spatial blurring by the diffuse imaging method.

3. Results

3.1. Effect of grid choice and the mean time data type

The resolution and spatial accuracy of the image reconstruction was studied using small absorbing perturbations. Three pairs of spherical target perturbations were introduced into the model with center-to-center distances 9.5 mm (pair D10), 13.8 mm (pair D14) and 17.3 mm (pair D17). The radius of each perturbation was 4.3 mm, and the absorption contrast compared to the background was $\Delta\mu_a = 0.008\ \mathrm{mm}^{-1}$. We limited the target perturbations to the gray and white matter of the brain, but no anatomical constraint was used in the reconstructions. Reconstructions were performed both using the intensity and mean time data types and using the intensity data type alone. Perfect knowledge of the background optical properties was assumed.

Transaxial slices through the centers of the target perturbations and tangential maps (explained below) calculated from the reconstructed images are shown in figure 2, and numerical data are given in table 2. The transaxial slice images show the depth performance of the reconstruction, whereas the tangential maps represent 2D maps of μ_{a} changes on the cortex. The peaks of the reconstructed perturbations may not be at the level of the transaxial slice, therefore the peak contrast shown in the slice may differ from that given in table 2.

For creating the tangential map, the mean value of the 3D data in the direction normal to the surface was calculated between depths 3.5 mm and 12 mm for each voxel of the tissue surface. The depth limits were chosen so that the superficial limit corresponded to the

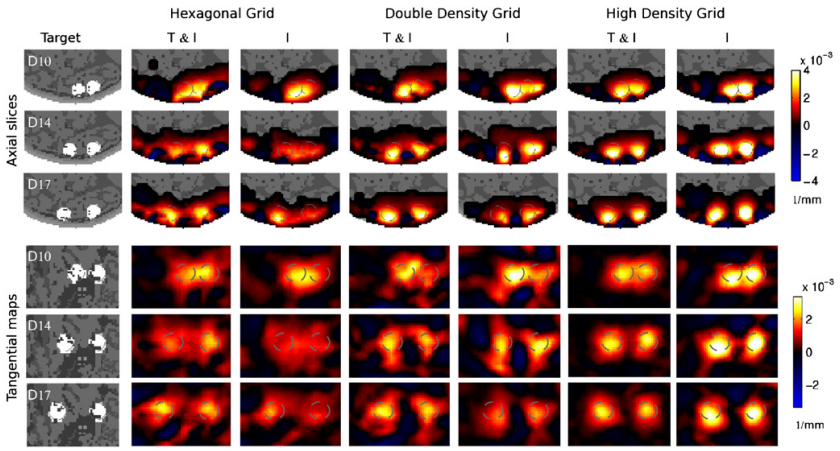

Figure 2. Reconstructions of two target perturbations at three different relative positions D10, D14 and D17. 'T&I' refers to the use of both mean time and intensity data types; 'I' refers to the use of the intensity data type alone. Above, axial slices of the reconstruction through the center of the target perturbations are shown, superimposed on the anatomical structure. Below, a tangential map calculated from the data is shown. The locations of the target perturbations are shown with dashed circles.

minimum depth at which the cortex begins in the region of the perturbations, and the deep limit lies near the deeper end of the target perturbations. Due to the averaging, the tangential maps have lower peak contrast than the axial images. The tangential maps show the spatial accuracy of the 3D reconstructions in the direction parallel to the scalp.

The best results were obtained with the HD grid. The reconstructions from intensity data alone had good spatial accuracy, which was further improved when the mean time data were also used. With the hexagonal grid, the reconstruction of case D14 produced poor image quality, whereas the DD grid was able to image the two perturbations successfully. In cases D10 and D17, the hexagonal and DD grids produced roughly comparable image quality. The use of mean time data in addition to intensity improved the image quality especially with the less dense grids. In all the cases where the two perturbations could be identified as distinct features, the use of mean time data improved the localization accuracy.

A noteworthy feature in the reconstructions presented here is the negative changes which were not included in the simulation. They are likely to be the result of noise in the simulated data and the rather sparse measurements probing the superficial tissues (skin and skull) due to the finite probe density. The negative absorption changes appear close to correctly reconstructed positive absorption changes and close to the edge of the imaging area where fewer overlapping measurements are available. Negative changes may also be seen in hemoglobin activation maps for physiological reasons. The region which appears negative in the HbO_2 map may have a decreased level of activity. Alternatively, regions surrounding a volume of increased activity may suffer from the blood stealing effect, and appear as negative, as the circulatory system is a closed system. These physiological explanations should be considered along with the technical explanations given above when considering activation maps with negative regions.

Table 2. Localization error and contrast for reconstructions in figure 2. T&I = mean time and intensity data, I = intensity data only. QI = Quality index.

	Hexagonal grid											
	Left perturbation						Right perturbation					
	Loc. err. (mm)		Peak contr. (%)		QI		Loc. err. (mm)		Peak contr. (%)		QI	
Target pair (Distance)	T&I	I	T&I	I	T&I	I	T&I	I	T&I	I	T&I	I
D10 (9.5 mm)[a]	1.8	2.7	46.5	42.1	7.1	8.7	–	–	–	–	7.5	6.1
D14 (13.8 mm)	1.4	4.1	32.4	26.5	4.3	3.4	1.3	3.5	49.0	34.0	5.3	3.4
D17 (17.3 mm)	2.5	3.3	54.2	59.8	5.0	5.2	1.4	3.9	45.3	37.5	4.6	3.5
	Double-density grid											
	Left perturbation						Right perturbation					
	Loc. err. (mm)		Peak contr. (%)		QI		Loc. err. (mm)		Peak contr. (%)		QI	
Target pair (Distance)	T&I	I	T&I	I	T&I	I	T&I	I	T&I	I	T&I	I
D10 (9.5 mm)[b]	2.5	1.7	51.4	71.3	6.3	7.9	–	–	–	–	4.4	4.9
D14 (13.8 mm)	2.4	3.9	47.1	55.0	4.9	4.2	1.6	2.3	45.6	48.2	4.9	5.5
D17 (17.3 mm)	2.5	3.7	58.1	41.6	7.1	6.0	1.4	2.6	52.9	48.7	6.2	7.4
	High-density grid											
	Left perturbation						Right perturbation					
	Loc. err. (mm)		Peak contr. (%)		QI		Loc. err. (mm)		Peak contr. (%)		QI	
Target pair (Distance)	T&I	I	T&I	I	T&I	I	T&I	I	T&I	I	T&I	I
D10 (9.5 mm)[a]	1.8	1.1	55.0	66.5	12.2	9.4	–	–	–	–	10.7	9.9
D14 (13.8 mm)	2.1	2.4	53.4	64.5	10.0	8.3	1.7	1.9	60.2	79.0	10.1	9.3
D17 (17.3 mm)	2.5	2.7	58.9	64.0	10.8	8.0	1.4	2.2	55.8	73.3	9.5	8.6

[a] In the reconstructions with the hexagonal and HD grids, the perturbations were fused in case D10. For this case, the localization error and peak contrast are calculated by assuming that the two perturbations are one.
[b] In the reconstruction with the DD grid, the left perturbation dominated the reconstruction. The localization accuracy and peak contrast are given for the left perturbation only.

3.2. Effect of modeling

The significance of the accurate modeling of light propagation in the optically heterogeneous head was studied by performing reconstructions using six different models (A through G), with different deviations from the reference model which was used to generate the simulated data. With the hexagonal and DD grids, both mean time and intensity data types were used in the reconstructions of this section. With the HD grid, intensity data only were used. The HD grid was adapted from study by Zeff *et al* (2007), in which continuous-wave instrumentation was used.

In case A, the pMC reconstruction method and the anatomical reference model were used. Case B was identical to case A, except for the reduced scattering coefficient of the CSF, which was altered to the value 0.3 mm^{-1}. In case C, we explored the effect of inaccuracies in the optical parameters using the pMC model. We sampled the parameters from a normal distribution of the logarithm of μ_a and μ_s', setting the means at the correct parameters. The standard deviation for the logarithm of μ_s' and μ_a was log(1.8), except for the μ_s' of the white matter, the standard deviation of which was log(2.2). The standard deviations correspond to deviations from −44% to +80% and from −56% to +120%, respectively. Results and parameter values are given for a representative example.

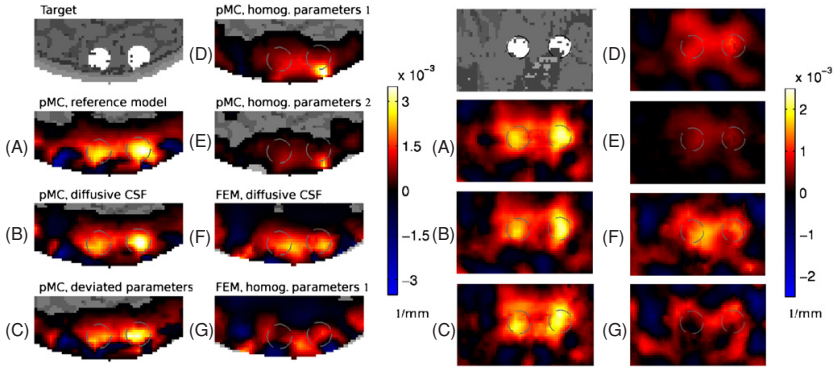

Figure 3. Reconstruction results obtained using different light propagation models and background optical properties with the hexagonal grid. Transaxial slices of the 3D solution are shown on the left, tangential maps on the right. Cases A through G are described in the text and summarized in table 3. Short descriptions detailing the computational model (pMC or FEM/DA) and the background model used are given above the transaxial slices.

Table 3. The reconstruction models studied, with optical parameters (GM = gray matter, WM = white matter, BG = background).

Case	A		B		C		D		E		F		G	
Model	pMC		pMC		pMC		pMC		pMC		FEM		FEM	
BG	Ref. params.		Diff. CSF		Dev. params.		Homog. 1		Homog. 2		Ref. params.[a]		Homog. 1	
Param.	μ_s'	μ_a	μ_s'	μ_a	μ_s'	μ_a	μ_s'	μ_a	μ_s'	μ_a	μ_s'	μ_a	μ_s'	μ_a
Scalp	1.9	0.018	1.9	0.018	3.82	0.011	1.33	0.018	1.6	0.02	1.9	0.018	1.33	0.018
Skull	1.6	0.016	1.6	0.016	0.78	0.031	1.33	0.018	1.6	0.02	1.6	0.016	1.33	0.018
GM	0.5	0.048	0.5	0.048	0.49	0.033	1.33	0.018	1.6	0.02	0.5	0.048	1.33	0.018
WM	1.0	0.037	1.0	0.037	0.88	0.047	1.33	0.018	1.6	0.02	1.0	0.037	1.33	0.018
CSF	0.032	0.004	0.3	0.004	0.012	0.005	1.33	0.018	1.6	0.02	0.3	0.004	1.33	0.018

[a] Parameters as closely the same as in the reference model as the resolution of the FE mesh allows. The exception is the CSF which is diffusive.

In cases D and E, the pMC model with homogeneous parameters was used. Two different cases are shown to demonstrate the dependence of the recovered contrast on the choice of the parameters.

In cases F and G, the FEM model with heterogeneous and homogeneous background optical properties were used, respectively. The heterogeneous parameters were the same as in the reference model, as closely as the accuracy of the FE mesh allowed. The homogeneous parameters were the same as in case D.

The different models, with the background optical parameters, are tabulated in table 3.

The results for the hexagonal grid are shown in figure 3, for the DD grid in figure 4 and for the HD grid in figure 5. Corresponding numerical data are given in table 4.

With all three optode grids, the results obtained using the pMC method with heterogeneous anatomical models (cases A, B and C) produced the best results. The approximate modeling of the CSF in case B changed the images very little. With the hexagonal grid, the perturbation on the left appears weaker in the images, but the numerical parameters show no significant deterioration. In case C, the deviated optical parameters resulted in some deterioration in the

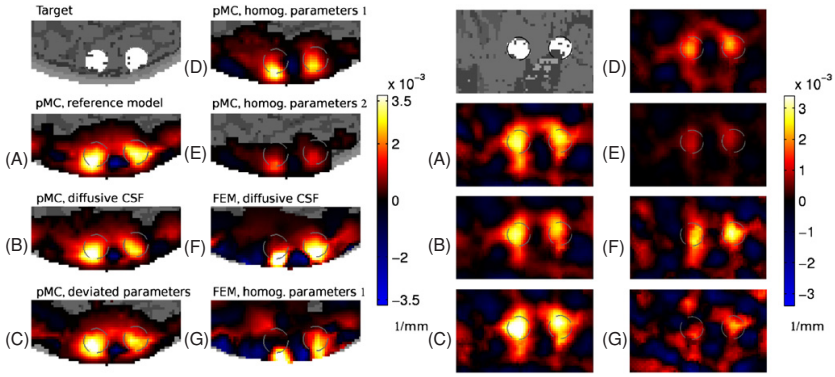

Figure 4. Reconstruction results obtained with the DD grid. Axial slices on the left, tangential maps on the right. Cases A through G as in figure 3.

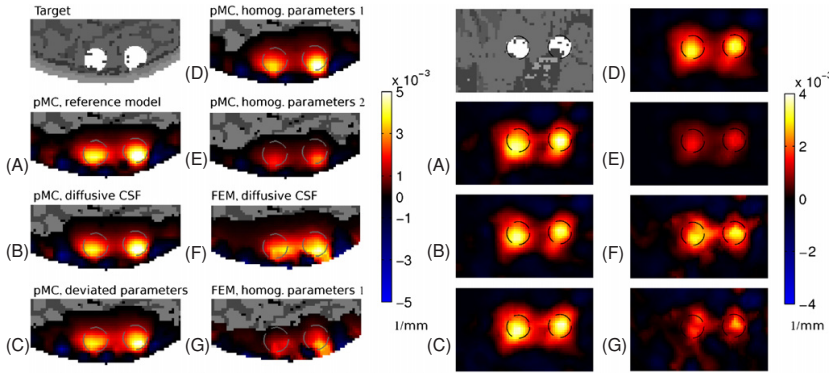

Figure 5. Reconstruction results obtained with the HD grid. Axial slices on the left, tangential maps on the right. Cases A through G as in figure 3.

images, but the contrast and localization of the reconstructed perturbations remained similar to those obtained using the reference optical properties. The result presented is a representative of a number of tests using similarly deviated parameters.

Using homogeneous models with pMC (cases D and E) resulted in inferior image quality compared to the heterogeneous models. The reconstruction results obtained with the hexagonal grid were poor in terms of both contrast and localization of the perturbations. With the DD and HD grids, the results were better, but the localization was inaccurate in the depth direction. The very different contrast recovery obtained with the two different sets of homogeneous parameters demonstrates the sensitivity of the reconstruction to the choice of background optical parameters. However, the spatial accuracy was very similar with both sets of homogeneous parameters.

Table 4. Reconstruction results for a pair of perturbations at a close (14 mm center-to-center) separation obtained using different models. QI = Quality index. Dashes in place of localization error and peak contrast indicate the perturbation was not reconstructed.

	Hexagonal grid					
	Left perturbation			Right perturbation		
Case	Loc. err. (mm)	Peak contr. (%)	QI	Loc. err. (mm)	Peak contr. (%)	QI
A	1.4	32.4	4.3	1.3	49.0	5.3
B	2.1	35.9	4.2	0.9	44.6	5.4
C	2.0	32.8	4.7	1.3	44.0	5.7
D	3.7	19.3	2.8	5.4	63.0	3.2
E	4.0	11.2	3.0	5.2	34.2	2.7
F	4.2	31.8	2.6	3.5	32.1	2.4
G	–	–	0.7	6.2	25.0	1.4
	Double-density grid					
	Left perturbation			Right perturbation		
Case	Loc. err. (mm)	Peak contr. (%)	QI	Loc. err. (mm)	Peak contr. (%)	QI
A	2.4	47.1	4.9	1.6	45.6	4.9
B	3.2	50.1	4.5	2.4	44.9	5.8
C	2.2	49.7	4.7	1.6	42.0	5.7
D	5.0	45.0	3.1	3.8	34.6	3.6
E	4.9	23.5	3.7	4.6	15.9	3.2
F	5.0	87.0	2.8	2.5	54.7	2.5
G	6.2	59.0	2.4	4.4	41.1	2.7
	High density grid					
	Left perturbation			Right perturbation		
Case	Loc. err. (mm)	Peak contr. (%)	QI	Loc. err. (mm)	Peak contr. (%)	QI
A	2.4	64.5	8.3	1.9	79.0	9.3
B	2.9	61.0	7.7	2.0	73.3	8.6
C	2.7	58.6	8.0	2.3	74.0	8.8
D	3.1	53.9	6.9	2.5	65.0	8.1
E	3.5	31.2	7.0	2.8	34.1	8.2
F	3.3	54.7	5.8	2.0	61.9	6.4
G	5.4	43.2	2.8	3.9	47.9	4.2

The reconstruction results obtained using the FEM/DA model (cases F and G) were very different for the three optode grids. With the hexagonal grid, the reconstruction using the heterogeneous parameters localized the perturbation on the left incorrectly between the two perturbations, and the reconstruction using the homogenous parameters failed altogether. With the DD grid, both perturbations were successfully reconstructed, although the depth localization was poor especially using homogeneous parameters. With the HD grid, both perturbations were reconstructed but the depth localization and the shape of the reconstructed perturbations in the axial image were poor, especially in the case of homogeneous parameters. The contrast and the QI were higher in the case of the heterogeneous parameters.

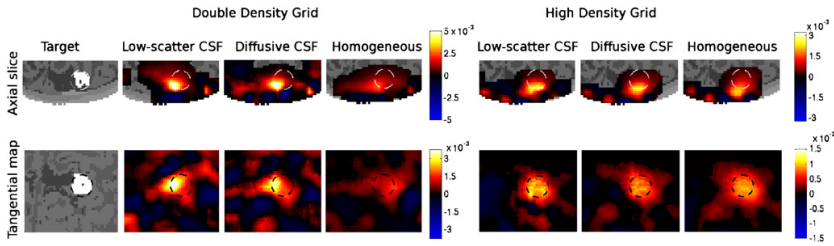

Figure 6. Reconstruction results in a case of a perturbation adjacent to a large region of CSF are shown. Upper row shows axial slices through the center of the perturbation, lower row shows tangential maps. The CSF is shown in dark gray. In the correct low-scattering case, $\mu'_{s,CSF} = 0.032\ mm^{-1}$, and in the diffusive case, $\mu'_{s,CSF} = 0.3\ mm^{-1}$.

Table 5. Reconstruction results for a perturbation adjacent to a region of CSF. QI = Quality index.

	DD grid			HD grid		
Case	Loc. err. (mm)	Peak contr. (%)	QI	Loc. err. (mm)	Peak contr. (%)	QI
Low-scattering CSF	3.3	81	4.3	3.5	37	3.6
Diffusive CSF	3.4	75	3.2	3.7	33	3.6
Homogeneous	7.4	22	2.6	5.1	27	3.4

3.3. Significance of the CSF model

As a final example, we studied the case of a single perturbation adjacent to a region of CSF between the cerebral hemispheres. In the reference model, the falx cerebri was given the optical properties of the skull, leaving a free space of CSF which we assumed to be low scattering.

The pMC model was used with the DD and HD optode arrangements. As in section 3.2, with the DD grid, both mean time and intensity data were used, and with the HD grid only intensity data were used. We reconstructed the perturbation using three different models for the background optical properties. These were (1) optical properties of the reference model (case A in table 3), (2) optical properties of the reference model, but with weakly diffusive CSF (case B in table 3) and (3) homogeneous optical properties (case D in table 3).

The reconstruction results are shown in figure 6. The axial slices are shown in the top row. The tangential maps shown in the bottom row were calculated from the data between the depths 6 mm and 14 mm. This corresponds approximately to the position of the target perturbation, the lower limit being 1 mm more superficial than the superficial limit of the target.

Using both optode grids, slightly higher contrast and better localization were achieved when the CSF was modeled correctly, but the difference to the results obtained with the weakly diffusive approximation was small in both cases. The results using the homogeneous optical parameters were significantly poorer, especially in the case of the DD grid. The localization error, peak contrast and QI of the reconstructions are given in table 5.

The dense optode array of the HD grid allowed good localization of the perturbations parallel to the scalp, but the depth localization was inaccurate. The percentage of contrast

that was recovered was low. This is probably due to the dominance of the measurements with short source–detector separations which have high SNR. With the DD grid, the localization of the reconstructed perturbations was less accurate parallel to the scalp, but a higher percentage of the contrast was recovered, and the depth localization was more accurate. We performed the reconstruction with the DD grid also without mean time data and the optical properties of the reference model. The localization error in this case was 4.2 mm, the peak contrast was 51%, and the QI was 4.2.

The result shows that adequate modeling of the CSF can be important for accurate reconstruction of localized absorption changes. In the case of regions of CSF that are larger than a very thin layer but smaller than 1 cm in dimension, the diffusive but low μ_s' as suggested by Custo *et al* (2006) is adequate. The CSF regions can play an even more significant part in light propagation in prematurely born infants with larger CSF spaces.

4. Discussion

In this paper, image reconstruction from diffuse optical imaging of activations in the neonatal brain was studied using Monte Carlo simulations. Specifically, we used MC to investigate the effect of the background optical properties, the availability of time-resolved information and the choice of the optode grid on the quality of reconstructed images. Hemodynamic activations were represented by local absorption changes in the MC model. In order to see the localization accuracy of the reconstructions, we used small absorbing perturbations with a contrast that was slightly higher than what is expected based on adult PET studies. Noise in the simulated data was comparable in magnitude with noise observed in physiological measurements of infants.

Our results suggest that adequate knowledge and modeling of the background optical properties and the use of time-resolved information can significantly improve the spatial accuracy of reconstructed images and make the recovery of contrast of absorption changes more consistent over simplified modeling of the background and the use of intensity data only. These factors can even be critical for the success of the reconstruction when the contrast in the signal is close to the noise level of the measurement. The contrast of the reconstructed perturbations was sensitive to the background optical properties used. To improve the quantitative accuracy of optical imaging, accurate *a priori* information on the tissue optical properties is needed. In addition, methods based on nonlinear optimization should be developed to minimize the difference between the model parameters and the true optical properties of the subject.

Of the factors studied, the density of the optode grid was found to have the greatest effect on image quality. If mean time data are available, it can improve spatial accuracy with all the grids studied. The high-density grid was found to give good spatial accuracy in the tangential maps even when large modeling errors were introduced. However, depth localization was found to be very sensitive to accurate modeling.

Localization accuracy was very good (typically, the localization error was less than 2.5 mm) when pMC was used with the correct background properties. Deviations in the optical properties were introduced into the model in accordance with expected subject-to-subject variability in the optical properties (based on variability reported in Franceschini *et al* (2007)). The spatial accuracy of the reconstructions remained good when the deviated parameters were used, and the percentage of recovered contrast changed very little ($<10\%$) with the DD and HD grids. The parameter values were drawn independently from a Gaussian distribution centered around the reference values of the model, and therefore the results may change if the errors in the optical parameters of the different tissues are correlated.

The reconstructions using the FEM/DA were successful in most cases (see figures 3–5), but better spatial accuracy and resolution was achieved with pMC, even when errors were introduced into the background optical properties. pMC allows precise anatomical information to be used and is not limited to tissues with high scattering. In some cases, with the DD and HD grids, the positions of the perturbations were reconstructed very close to the surface of the tissue by the FEM/DA method. This illustrates the possible errors that may be introduced by the use of approximate methods such as the FEM/DA. Since MC was used to generate the simulated data, the result does not indicate that pMC is superior as a reconstruction method.

Precise anatomical information of the internal structure of the head is usually not available for healthy infants. We believe that this problem can to some extent be alleviated by using a library of segmented anatomical MR images obtained from infants of the same age as the subject. The boundary shape can be measured, e.g., using photogrammetry (Gibson *et al* 2003) or other digitization methods such as the Polhemus pen and the library images can then be deformed to match the shape of the head of the subject.

5. Conclusions

Of the parameters studied, the optode density was found to have the greatest effect on image quality. For imaging of brain activation in neonates, the optode grid should have a spatial sensitivity pattern which is as even as possible, and there should be multiple overlapping measurements covering the region of interest.

The addition of the mean time data type improved the spatial accuracy and consistency of the reconstructed images. In order to gain full advantage of the use of temporal data types, the instrumentation should combine a wide dynamic range allowing measurements using a dense multidistance optode grid with a good signal-to-noise ratio and a short imaging time. These characteristics have yet to be achieved in a TD or an FD system.

The background optical parameters used in the light propagation model should be chosen with care to obtain consistent reconstructions. Nonlinear techniques may allow the reconstruction of the model parameters when some spatial *a priori* information of the internal structure is available. Currently, nonlinear Monte Carlo techniques are prohibitatively expensive in terms of the time of computation required. The FEM/DA with nonlinear optimization is fast, but further attention should be put into understanding the implications of the approximations made in the FEM/DA model and optimizing the accuracy of the forward model when measurements using short ($\sim$10 mm) source–detector separations are included in the data.

Of particular importance is the modeling of regions of CSF that are greater in extent than a thin layer. The use of a spatially accurate model and a low diffusion coefficient for the CSF resulted in good reconstructions, when such regions were present close to the absorptive perturbation.

Acknowledgments

The authors wish to acknowledge the help of Ellen P Grant of Massachusetts General Hospital in providing the MR data used in this work and Simon Arridge of University College London for useful discussions. The use of computation facilities of Genome Informatics Unit, Biomedicum Helsinki (http://www.giu.fi) is gratefully acknowledged. This work was financially supported by the Finnish Cultural Foundation, the Biomedicum Helsinki Foundation, the Instrumentarium Foundation, the KAUTE Foundation, the Alfred Kordelin

Foundation, the Finnish Academy of Science and Letters, and the Academy of Finland (project number 120946).

References

Arridge S R 1995 Photon-measurement density-functions: I. Analytical forms *Appl. Opt.* **34** 7395–409

Arridge S R 1999 Optical tomography in medical imaging *Inverse Problems* **15** R41–93

Arridge S R and Lionheart W R B 1998 Nonuniqueness in diffusion-based optical tomography *Opt. Lett.* **23** 882–4

Arridge S R, Schweiger M, Hiraoka M and Delpy D T 1993 A finite element approach for modeling photon transport in tissue *Med. Phys.* **20** 299

Bazaraa M S, Sherali H D and Shetty C M 1993 *Nonlinear Programming: Theory and Algorithms* (New York: Wiley)

Björck A 1996 *Numerical Methods for Least Squares Problems* (Philadelphia, PA: Society for Industrial and Applied Mathematics)

Boas D A, Chen K, Grebert D and Franceschini M A 2004 Improving the diffuse optical imaging spatial resolution of the cerebral hemodynamic response to brain activation in humans *Opt. Lett.* **29** 1506

Boas D A, Culver J P, Stott J J and Dunn A K 2002 Three dimensional Monte Carlo code for photon migration through complex heterogenous media including the adult human head *Opt. Exp.* **10** 159

Boas D A and Dale A M 2005 Simulation study of magnetic resonance imaging-guided cortically constrained diffuse optical tomography of human brain function *Appl. Opt.* **44** 1957–68

Boas D A, Dale A M and Franceschini M A 2004 Improving the diffuse optical imaging spatial resolution of the cerebral hemodynamic response to brain activation in humans *Opt. Lett.* **29** 1506

Chance B *et al* 1998 A novel method for fast imaging of brain function, non-invasively, with light *Opt. Exp.* **2** 411–23

Chandrasekhar S 1960 *Radiative Transfer* (New York: Dover)

Custo A, Wells W M III, Barnett A H, Hillman E M C and Boas D A 2006 Effective scattering coefficient of the cerebral spinal fluid in adult head models for diffuse optical imaging *Appl. Opt.* **45** 4747–55

Dehghani H, Arridge S R, Schweiger M and Delpy D T 2000 Optical tomography in the presence of void regions *J. Opt. Soc. Am.* A **17** 1659–70

Dehghani H and Delpy D T 2002 Linear single-step image reconstruction in the presence of nonscattering regions *J. Opt. Soc. Am.* A **19** 1162–71

Firbank M, Arridge S R, Schweiger M and Delpy D T 1996 An investigation of light transport through scattering bodies with non-scattering regions *Phys. Med. Biol.* **41** 767–83

Franceschini M A, Thaker S, Themelis G, Krishnamoorthy K K, Bortfeld H, Diamond S G, Boas D A, Arvin K and Grant P E 2007 Assessment of infant brain development with frequency-domain near-infrared spectroscopy *Pediatr. Res.* **61** 546–51

Fukui Y, Ajichi Y and Okada E 2003 Monte Carlo prediction of near-infrared light propagation in realistic adult and neonatal head models *Appl. Opt.* **42** 2281

Gibson A P, Austin T, Everdell N L, Schweiger M, Arridge S R, Meek J H, Wyatt J S, Delpy D T and Hebden J C 2006 Three-dimensional whole-head optical tomography of passive motor evoked responses in the neonate *Neuroimage* **30** 521–8

Gibson A P, Hebden J C, Riley J, Everdell N, Schweiger M, Arridge S R and Delpy D T 2005 Linear and nonlinear reconstruction for optical tomography of phantoms with nonscattering regions *Appl. Opt.* **44** 3925–36

Gibson A P, Riley J, Schweiger M, Hebden J C, Arridge S R and Delpy D T 2003 A method for generating patient-specific finite element meshes for head modelling *Phys. Med. Biol.* **48** 481–95

Hämäläinen M, Hari R, Ilmoniemi R J, Knuutila J and Lounasmaa O V 1993 Magnetoencephalography—theory, instrumentation, and applications to noninvasive studies of the working human brain *Rev. Mod. Phys.* **65** 413–97

Hayakawa C, Spanier J, Bevilacqua F, Dunn A, You J, Tromberg B and Venugopalan V 2001 Perturbation Monte Carlo methods to solve inverse photon migration problems in heterogeneous tissues *Opt. Lett.* **26** 1335

Hebden J C, Gibson A, Austin T, Yusof R, Everdell N, Delpy D T, Arridge S R, Meek J H and Wyatt J S 2004 Imaging changes in blood volume and oxygenation in the newborn infant brain using three-dimensional optical tomography *Phys. Med. Biol.* **49** 1117–30

Hebden J C, Gibson A, Yusof R, Everdell N, Hillman E M C, Delpy D T, Arridge S R, Austin T, Meek J H and Wyatt J S 2002 Three-dimensional optical tomography of the premature infant brain *Phys. Med. Biol.* **47** 4155–66

Heiskala J, Kotilahti K, Lipiäinen L, Hiltunen P, Grant P E and Nissilä I 2007 Optical tomographic imaging of activation of the infant auditory cortex using perturbation Monte Carlo with anatomical *a priori* information *Proc. SPIE Diffuse Optical Imaging in Tissue (Munich)* vol 6629 (Bellingham, WA: SPIE) p 66290T

Heiskala J, Nissilä I, Neuvonen T, Järvenpää S and Somersalo E 2005 Modeling anisotropic light propagation in a realistic model of the human head *Appl. Opt.* **44** 2049

Hiraoka M, Firbank M, Essenpreis M, Cope M, Arridge S R, van der Zee P and Delpy D T 1993 A Monte Carlo investigation of optical pathlength in inhomogeneous tissue and its application to near-infrared spectroscopy *Phys. Med. Biol.* **38** 1859–76

Homae F, Watanabe H, Nakano T and Taga G 2007 Prosodic processing in the developing brain *Neurosci. Res.* **59** 29–39

Kacprzak M, Liebert A, Sawosz P, Zolek N and Maniewski R 2007 Time-resolved optical imager for assessment of cerebral oxygenation *J. Biomed. Opt.* **12** 034019

Kawaguchi H, Koyama T and Okada E 2007 Effect of probe arrangement on reproducibility of images by near-infrared topography evaluated by a virtual head phantom *Appl. Opt.* **46** 1658–68

Kotilahti K, Nissilä I, Huotilainen M, Mäkelä R, Gavrielides N, Noponen T, Björkman P, Fellman V and Katila T 2005 Bilateral hemodynamic responses to auditory stimulation in newborn infants *Neuroreport* **46** 1373–7

Kumar P and Vasu R M 2004 Reconstruction of optical properties of low-scattering tissue using derivative estimated through perturbation Monte-Carlo method *J. Biomed. Opt.* **9** 1002

Liebert A, Wabnitz H, Steinbrink J, Obrig H, Möller M, Macdonal R, Villringer A and Rinneberg H 2004 Time-resolved multidistance near-infrared spectroscopy of the adult head: intracerebral and extracerebral absorption changes from moments of distribution of times of flight of photons *Appl. Opt.* **43** 3037–47

Meek J H, Firbank M, Elwell C E, Atkinson J, Braddick O and Wyatt J S 1998 Regional haemodynamic responses to visual stimulation in awake infants *Pediatr. Res.* **42** 840–3

Nissilä I *et al* 2006 Comparison between a time-domain and a frequency-domain system for optical tomography *J. Biomed. Opt.* **11** 064015

Nissilä I, Kotilahti K, Fallström K and Katila T 2002 Instrumentation for the accurate measurement of phase and amplitude in optical tomography *Rev. Sci. Insrum.* **73** 3306

Nissilä I, Noponen T, Kotilahti K, Katila T, Lipiäinen L, Tarvainen T, Schweiger M and Arridge S 2005 Instrumentation and calibration methods for the multichannel measurement of phase and amplitude in optical tomography *Rev. Sci. Instrum.* **76** 044302

Okada E, Firbank M, Schweiger M, Arridge S R, Cope M and Delpy D T 1997 Theoretical and experimental investigation of near-infrared light propagation in a model of the adult head *Appl. Opt.* **36** 21–31

Otskuka Y, Nakato E, Kanazawa S, Yamaguchi M K, Watanabe S and Kakigi R 2007 Neural activation to upright and inverted faces in infants measured by near infrared spectroscopy *Neuroimage* **34** 399–406

Prahl S A, Keijzer M, Jacques S L and Welch A J 1989 A Monte Carlo model of light propagation in tissue *Dosimetry of Laser Radiation in Medicine and Biology* (*SPIE Int. Series IS* vol 5) ed G J Müller and D H Sliney (Bellingham, WA: SPIE) pp 102–11

Ren K, Abdoulaev G S, Bal G and Hielscher A H 2004 Algorithm for solving the equation of radiative transfer in the frequency domain *Opt. Lett.* **29** 578–80

Riley J, Dehghani H, Schweiger M, Arridge S R, Ripoll J and Nieto-Vesperinas M 2000 3D optical tomography in the presence of void regions *Opt. Exp.* **7** 462–7

Rosen B R, Aronen H J, Kwong K K, Belliveau J W, Hamberg L M and Fordham J A 1993 Advances in clinical neuroimaging—functional MR-imaging techniques *Radiographics* **13** 889–96

Schmidt F 1999 Development of a time-resolved optical tomography system for neonatal brain imaging *PhD Thesis* University of London

Schmidt F E W, Fry M E, C, Hillman E M, Hebden J C and Delpy D T 2000 A 32-channel time-resolved instrument for medical optical tomography *Rev. Sci. Instrum.* **71** 256–65

Schweiger M, Arridge S R, Hiraoka M and Delpy D T 2005 The finite element method for the propagation of light in scattering media: boundary and source conditions *Med. Phys.* **22** 1779–92

Schweiger M, Arridge S R and Nissilä I 2005b Gauss–Newton method for image reconstruction in diffuse optical tomography *Phys. Med. Biol.* **50** 2365–86

Seghier M L, Lazeyras F and Huppi P S 2006 Functional MRI of the newborn *Semin. Fetal Neonatal Med.* **11** 479–88

Selb J, Joseph D K and Boas D A Time-gated optical system for depth-resolved functional brain imaging *J. Biomed. Opt.* **11** 044008

Steinbrink J, Wabnitz H, Obrig H, Villringer A and Rinneberg H 2001 Determining changes in NIR absorption using a layered model of the human head *Phys. Med. Biol.* **46** 879–96

Tarvainen T, Vauhkonen M, Kolehmainen V, Arridge S R and Kaipio J P 2005 Coupled radiative transfer equation and diffusion approximation model for photon migration in turbid medium with low-scattering and non-scattering regions *Phys. Med. Biol.* **50** 4913–30

Toronov V, Webb A, Choi J H, Wolf M, Safanova L, Wolf U and Gratton E 2001 Study of local cerebral hemodynamics by frequency-domain near-infrared spectroscopy and correlation with simultaneously acquired functional magnetic resonance imaging *Opt. Exp.* **9** 417–27

Tsuchiya Y 2001 Photon path distribution and optical responses of turbid media: theoretical analysis based on the microscopic Beer–Lambert law *Phys. Med. Biol.* **46** 2067–84

Villringer A and Chance B 1997 Non-invasive optical spectroscopy and imaging of human brain function *Trends Neurosci.* **20** 435–42

Wang L, Jacques S L and Zheng L 1995 MCML–Monte Carlo modeling of light transport in multi-layered tissues *Comput. Methods Programs Biomed.* **47** 131

Wilcox T, Bortfeld H, Woods R, Wruch E and Boas D A 2005 Using near-infrared spectroscopy to assess neural activation during object processing in infants *J. Biomed. Opt.* **10** 011010

Zeff B W, White B R, Dehghani H, Schlaggar B L and Culver J P 2007 Retinotopic mapping of adult human visual cortex with high-density diffuse optical tomography *Proc. Natl. Acad. Sci.* **104** 12169–74